Appendix A. The FEM model

The equilibrium equation of a compressible, adiabatic and inviscid fluid for small perturbation is:

$$\nabla p_a + \rho(x) \cdot \ddot{u} = 0, \tag{A 1}$$

where p_a is the excess pressure in the fluid (the pressure in excess of the static pressure) and $\ddot{u}$ is the fluid acceleration. The constitutive behavior of the fluid is assumed to be inviscid, linear and compressible, therefore,

$$p_a = -K_f \nabla u, \tag{A 2}$$

where K_f is the bulk modulus of the fluid. We assume that all the variables of interest oscillate harmonically at an angular frequency of Ω ($f = \tilde{f} e^{i\Omega t}$). Using the harmonic time-derivative relations we obtain:

$$\nabla \tilde{p}_a - \Omega^2 \rho \tilde{u} = 0, \tag{A 3}$$

Combining the space derivative of Eq. (A 3) with Eq. (A 2), we obtain:

$$-\Omega^2 \frac{1}{K_f} \tilde{p}_a - \nabla \cdot \left(\frac{1}{\rho} \nabla \tilde{p}_a \right) = 0 \tag{A 4}$$

The FEM model accounts for scattering and multiple scattering. The fluid-structure acoustic model of ABAQUS couples the solid with the acoustic medium by equating the volumetric acceleration fluxes (Pierce 1991) at the interfaces.

Appendix B. Analytical solutions

For small radii, the axial force action on the particle increases as a function of R_s^3, as King predicted (Fig. S1a). For larger radii, when the standing wave condition is broken, the Hasegawa's solution for a travelling wave shows a different behavior from the numerical solutions (Hasegawa *et al.* 1980). This difference is likely due to the dimension of the emitter and reflector compared to the sphere. In fact, when a smaller flat reflector is used, the Hasegawa solution for travelling wave gives more precise results (Fig. S1b)

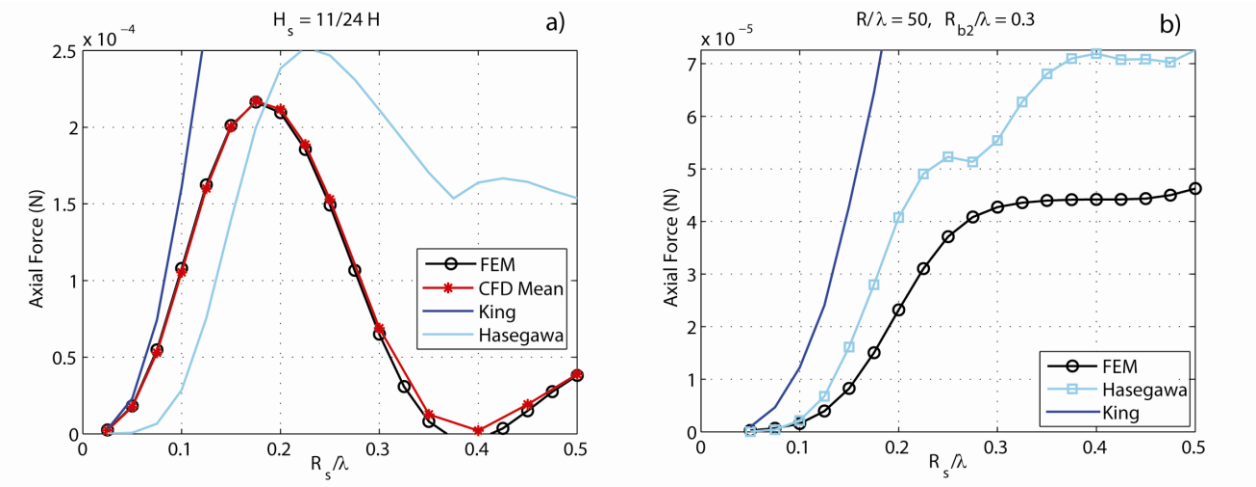

Figure S1 a) Axial force acting on a rigid sphere for different radii with the standard configuration and b) a smaller flat reflector.

Appendix C. The CFD model

The equations for conservation of mass and momentum are:

$$\frac{\partial \rho}{\partial t} + \nabla \cdot (\rho \vec{v}) = 0 \tag{C 1}$$

$$\frac{\partial}{\partial t}(\rho \vec{v}) + \nabla \cdot (\rho \vec{v}\vec{v}) = -\nabla p + \nabla \cdot (\bar{\bar{\tau}}) \tag{C 2}$$

where p is the static pressure, $\bar{\bar{\tau}}$ is the stress tensor is given by

$$\bar{\bar{\tau}} = \mu \left[(\nabla \vec{v} + \nabla \vec{v}^{T}) - \frac{2}{3} \nabla \cdot \vec{v} I \right] \tag{C 3}$$

where μ is the molecular viscosity and I is the unit tensor. For compressible flows, the ideal gas law is:

$$\rho = \frac{p}{\frac{R}{M_w} T} \tag{C 4}$$

where R is the universal gas constant and M_w is the molecular weight. The temperature, T, is computed from the energy equation.

$$\frac{\partial}{\partial t}(\rho E) + \nabla \cdot (\vec{v}(\rho E + p)) = \nabla \cdot (k \nabla T + (\bar{\bar{\tau}} \cdot \vec{v})) \tag{C 5}$$

$$E = \frac{v^2}{2} - \frac{p}{\rho} \qquad \text{(C 6)}$$

where k is thermal conductivity. The two terms on the right-hand side of Eq. (C 5) represent energy transfer due to conduction and viscous dissipation.

To solve the CFD model, a pressure-based solver was used, since it offers a better computational efficiency. On the other hand, the use of this solver imposes the use of a reflecting boundary condition (pressure outlet/inlet). To avoid interference with the core of the domain (inside the levitator), the domain (figure 1b) was extended accordingly by the number of periods required for the simulation to give a stable result (n_t). For example, if n_t =150, the radius of the external boundary with pressure outlet boundary condition was chosen longer than $150\lambda/2$ (in our case, 112.5λ). The added computational cost was relatively low (10-15%), since the cells become coarser as farther from the core of the levitator. The mesh was unstructured, with the exception of a boundary layer of structured mesh around the sphere.

Appendix D. The RMS pressure and velocity

The RMS pressure and velocity decrease with moving away from the central axis (figure S2).

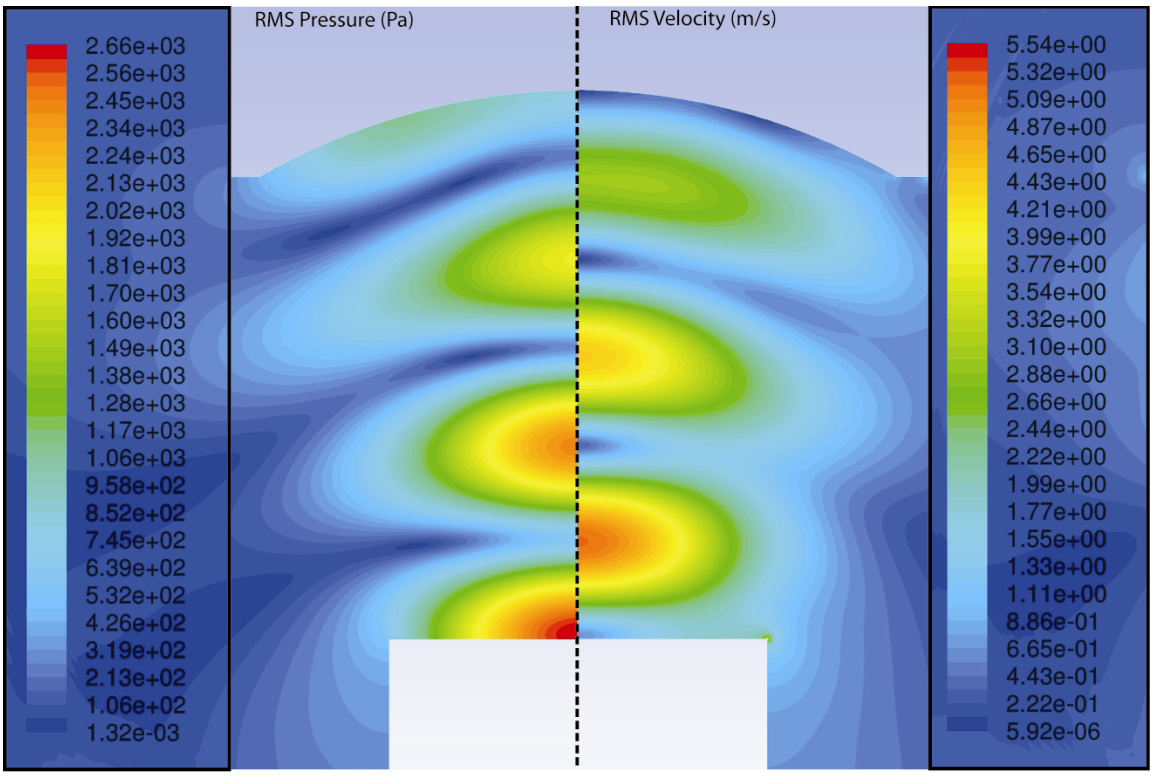

Figure S2 The RMS pressure (left) and velocity (right) in the axi-symmetric levitator for the inviscid case.

Appendix E. Asymptotic values

In figure S3, typical asymptotic value plots are shown. For small radii, the solution is periodic (figure S3, left). For large radii, the solutions show strong oscillations around the mean value of the radial force (figure S3, right).

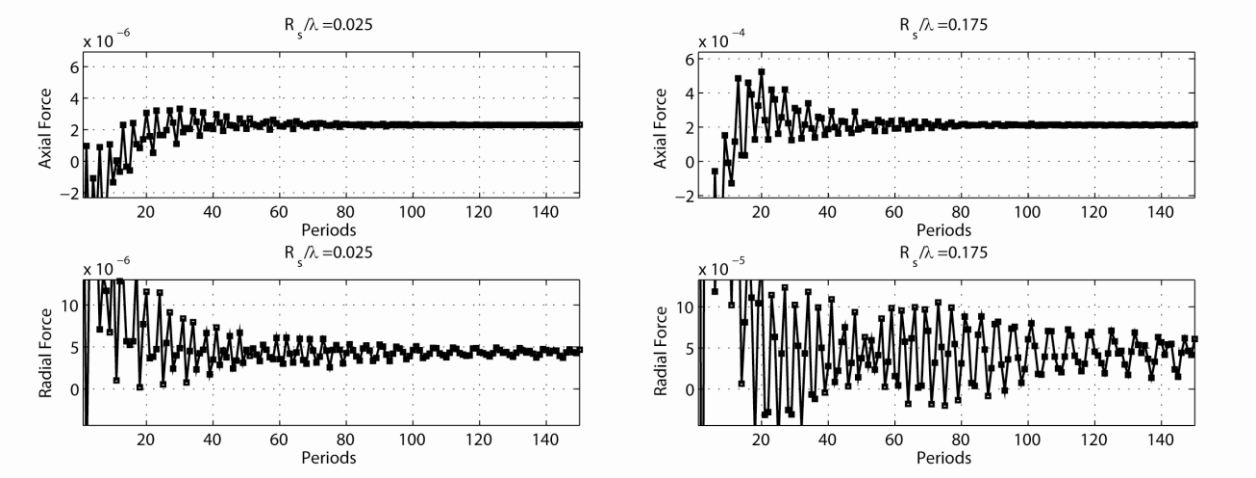

Figure S3. Asymptotic values of the axial and radial forces for small (R_s/λ= 0.025, left) and large (R_s/λ=0.175, right) radii. The axial force reaches its asymptotic value before 80th periods, while the radial force keeps oscillating until the end of the sampling (n_t=150).

Appendix F. The acoustic boundary layer

A boundary layer thickness comparable to the particle size is shown in figure S4 for R_s/λ =0.0025.

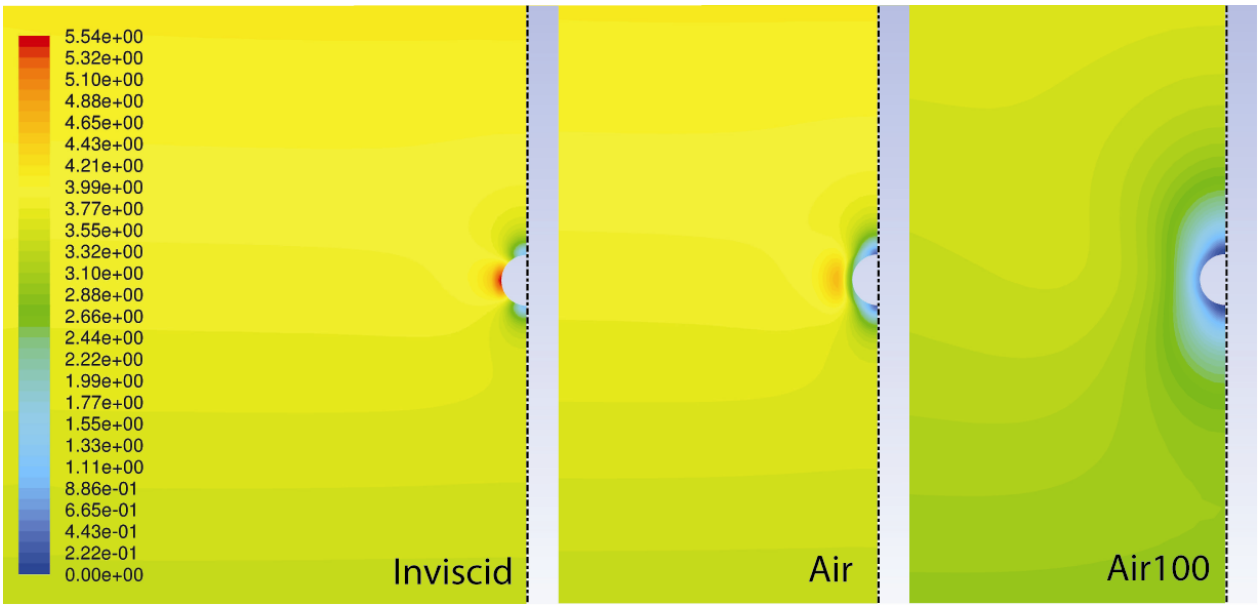

Figure S4. Contour plots of the RMS particle velocity v_{rms} (m/s) for R_s/λ = 0.0025 at different values of viscosity. It can be seen that already at air viscosity the boundary layer thickness is comparable with the particle size. The RMS value is obtained by averaging the periods 90 to 150.

A boundary layer thickness negligible compared to the particle size is shown in figure S5 for R_s/λ =0.3.

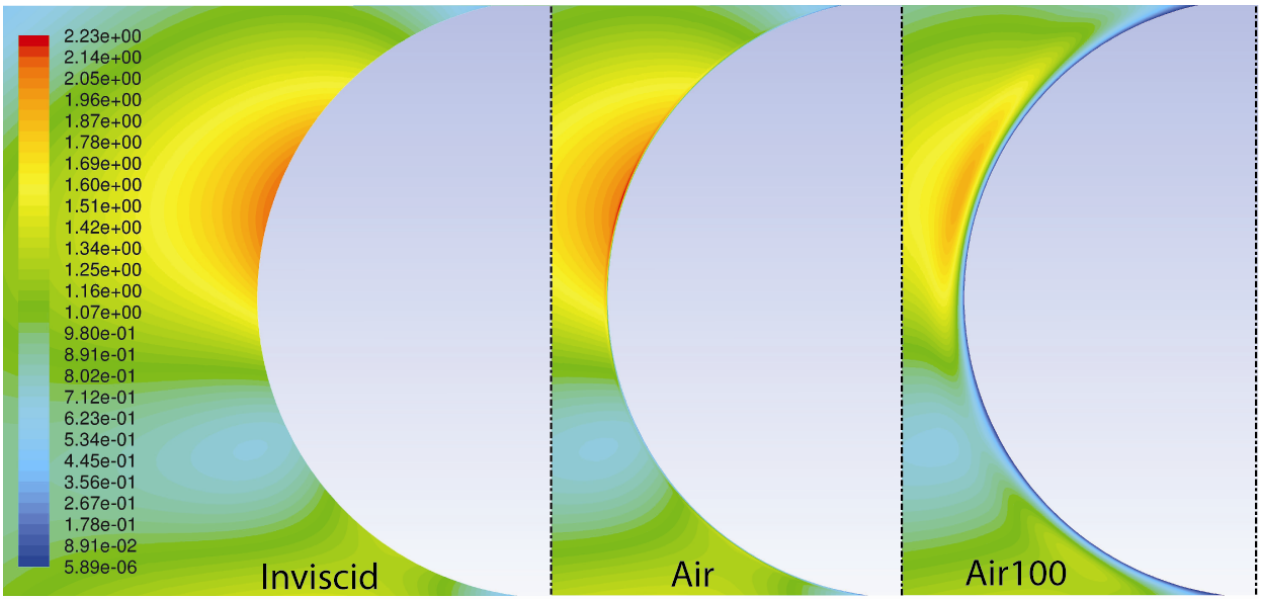

Figure S5 Contour plots of the RMS particle velocity v_{rms} (m/s) for R_s/λ = 0.3 at different viscosities.

Appendix G. The acoustic streaming

The small vortices at the upper and lower sides of the sphere are in the opposite directions than the streaming inside the boundary layer (figure S6). The streaming shows a similar pattern as in (Lee & Wang

1990; Ohsaka *et al.* 2002; Rednikov *et al.* 2006). The mean axial and radial velocities explain the opposite drag force contribution on the radial and axial forces.

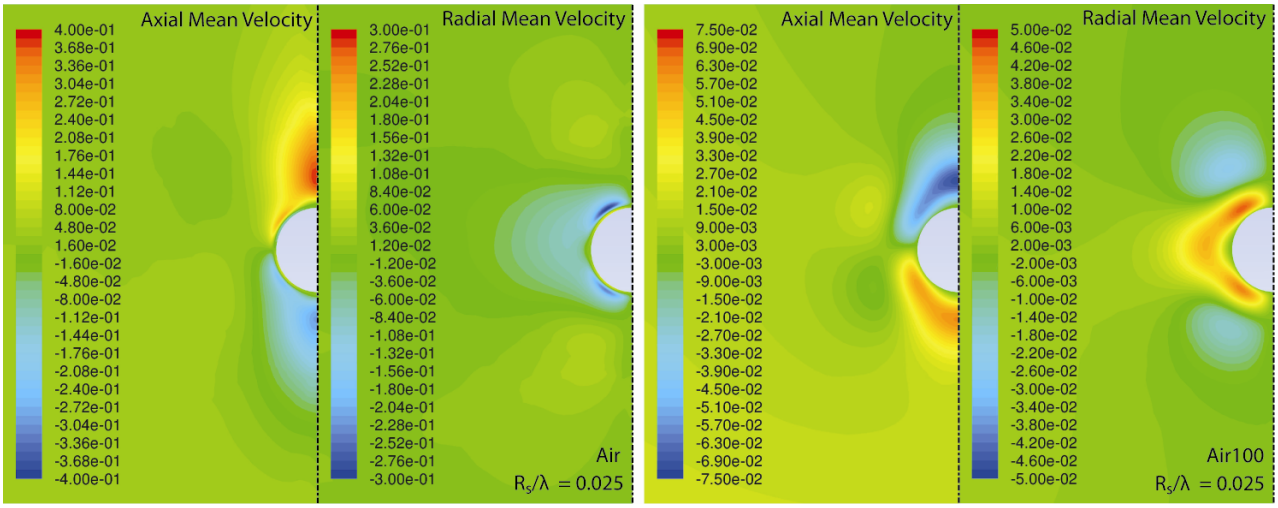

Figure S6 Mean axial and radial velocities for a sphere of R_s/λ = 0.025 with two viscosities (air and air100). For low viscosity, i.e. thin acoustic boundary layer, only the external acoustic streaming can be seen compared to the sphere size. When the viscosity increases, the acoustic streaming within the boundary layer is clearly visible. The mean value is obtained by averaging over the periods 90 to 150.

Appendix H. Effect of viscosity on big Radii

Viscosity reduced the radial force for negative values, i.e. it increases in magnitude. The results for R_s=0.3λ, (negative radial force, lowest relative difference with FEM in the big radii range, figure 3b) illustrate this behavior (Table S1).

Table S1. Values of Axial and Radial Force for R_s/λ = 0.3 at different viscosities.

	Axial Force (N)	Radial Force (N)
Inviscid	6.9256e-05	-2.0798e-05
Air	6.8328e-05	-2.0811e-05
Air100	5.7848e-05	-2.0933e-05

Appendix I. Ellipsoid

Values of b/λ for equivalent-volume sphere radii.

Table S2. Equivalent radius and semi-major axis of the ellipsoids.

R_s/λ	b/λ (b/a = 2)	b/λ (b/a = 5)

0.025	0.0315	0.0427
0.1	0.126	0.171
0.175	0.220	0.299

The RMS velocity significantly decreases with viscosity at the horizontal-axis extremities of the ellipsoid (figure S7).

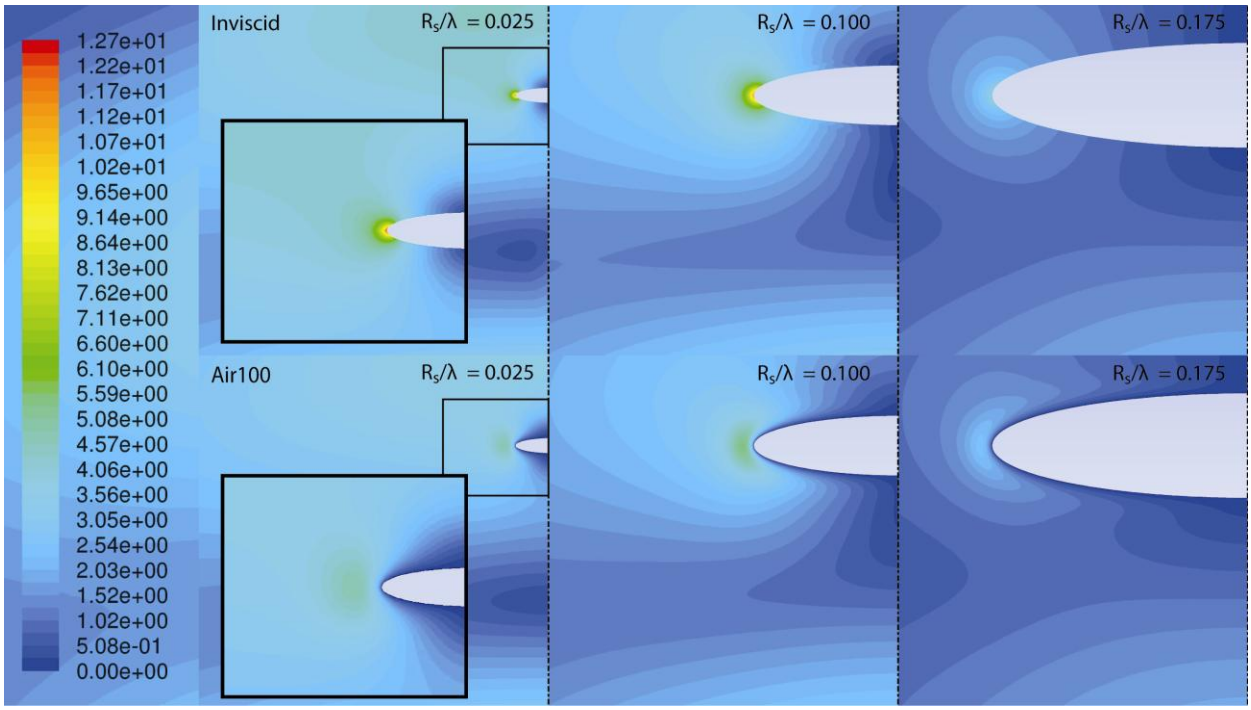

Figure S7 Contour plots of the RMS particle velocity v_{rms} (m/s) for ellipsoid (b/a = 5) of different radii and viscosities.

REFERENCES

HASEGAWA, T., M. OCHI and K. MATSUZAWA 1980 Acoustic Radiation Pressure on a Rigid Sphere in a Spherical Wave Field *J. Acoust. Soc. Am.* 67, 770-773.

LEE, C. P. and T. G. WANG 1990 Outer Acoustic Streaming *J. Acoust. Soc. Am.* 88, 2367-2375.

OHSAKA, K., A. REDNIKOV, S. S. SADHAL and E. H. TRINH 2002 Noncontact technique for determining viscosity from the shape relaxation of ultrasonically levitated and initially elongated drops 73, 2091-2096.

PIERCE, A. D. 1991 Acoustics - An introduction to its principle and applications

REDNIKOV, A. Y., H. ZHAO, S. S. SADHAL and E. H. TRINH 2006 Steady streaming around a spherical drop displaced from the velocity antinode in an acoustic levitation field *Q. J. Mech. Appl. Math.* 59, 377-397.